Robotica (2012) volume 30, pp. 491–503. © Cambridge University Press 2011
doi:10.1017/S0263574711000798

# Terramechanics-based wheel–terrain interaction model and its applications to off-road wheeled mobile robots

Zhenzhong Jia†,‡, William Smith†,‡ and Huei Peng†,‡,*

†*Department of Mechanical Engineering, University of Michigan, Ann Arbor, MI 48109, USA*
‡*Ground Robotics Reliability Center (GRRC), University of Michigan, Ann Arbor, MI 48109, USA*

(Accepted June 15, 2011. First published online: July 25, 2011)

**SUMMARY**

This paper presents a wheel–terrain interaction model, which enables efficient modeling of wheeled locomotion in soft soil and numerical simulations of off-road mobile robots. This modular model is derived based on wheel kinematics and terramechanics and the main focus is on describing the stress distributions along the wheel–terrain interface and the reaction forces exerted on the wheel by the soil. When the wheels are steered, the shear stresses underneath the wheel were modeled based on isotropic assumptions. The forces and torques contributed by the bulldozing effect of the side surfaces is also considered in the proposed model. Furthermore, the influence of grousers, commonly used on smaller mobile robots, was modeled by (1) averaging the normal pressures contributed by the grousers and the wheel concave portion, and (2) assuming that the shear phenomenon takes places along the grouser tips. By integrating the model with multibody system code for vehicle dynamics, simulation studies of various off-road conditions in three-dimensional environments can be conducted. The model was verified by using field experiment data, both for a single-wheel vehicle and a whole vehicle.

KEYWORDS: Wheel–terrain interaction; Wheel–soil interface; Terramechanics; Off-road mobile robots; Multibody system.

## 1. Introduction

Wheeled mobile robots and unmanned ground vehicles (UGVs) have many applications, including reconnaissance, surveillance, rescue, and planetary exploration. These applications often require the robots to travel on unstructured, rugged terrain to conduct tasks, such as surveillance or transporting material.[1] The mobility and trafficability of the robots in these off-road environments are crucial to the mission success, with a common failure mode being the robot trapped in soft soil. Another key mission factor is power consumption, which has become particularly relevant for applications with limited energy sources.[2] Thus, to achieve a successful mission and improve the overall robot mobility and power performance, efficient modeling of wheeled locomotion and propulsion load is required,[3] in which the wheel–terrain interaction plays an important role.

* Corresponding author. E-mail: hpeng@umich.edu

In the mid-20th-century, Bekker systematically studied the principles of off-road vehicle–terrain interaction[4,5] and laid the foundation for "terramechanics," which was later extended by Wong[6,7] to form an important element of off-road vehicle dynamics. In ref. [8], Wong proposed an analytical model to predict the performance of a driven rigid wheel on soft soil in a straight-line motion scenario. For the steering performance, a general theory for skid-steering tracked vehicles on flat firm ground[9] was proposed although the wheeled vehicles were not covered. One contribution of this tracked vehicle model is the identification of shear deformations and stress distributions along the track–soil interface during steady-turning maneuvers.

Inspired by Wong's work, Tran proposed a two-dimensional (2D) dynamic model of the vehicle–terrain interaction for a skid-steering wheeled UGV on a flat surface.[10,11] In the model, an integrated approach was utilized by expressing the soil deformations and reaction forces into the vehicle coordinate frame directly.[10] Model flexibility is an issue of this integrated approach since extensive work is required to fit this model into other vehicle configurations. Also, specific vehicle dynamic equations must be derived, which can be very complex for mobile robots, such as the Mars exploration rovers, with steering mechanisms or suspensions.

In refs. [12, 13], a terramechanics-based analytical model for the steering maneuvers of planetary exploration rovers on loose soil was developed. The model, which is termed "all-wheel dynamics model," used a separate approach and can be divided into two submodels: the "wheel–soil contact model," by which the contact forces on the wheel can be obtained; and the 'wheel-and-vehicle model', in which the forward dynamics was solved by the *Open Dynamics Engine* (ODE) and a multibody system (MBS) dynamics solver. Modeling of the wheel–soil interaction during a turning maneuver was achieved by linear motion approximation at different slip angles. The shear stress along the wheel–terrain interface was assumed to be anisotropic by assigning different values to the shear moduli along the longitudinal and the lateral directions.[13] This method leads to two underlying problems: (1) the direction of the shear stress is not strictly opposite to the shear velocity under most circumstances by using the anisotropic assumption; and (2) it is uncertain, however, that the longitudinal and lateral shear moduli can be experimentally measured. In addition, the influence of lugs/grousers, an important factor affecting

Table I. Comparison between WTIM and other wheel/track/vehicle–terrain interaction models.

| Model (ref.) | Wheel type | Package form | Model dimension | Method for the steering maneuver | Bulldozing effect included? | Model the grousers? | Numerical integration |
|---|---|---|---|---|---|---|---|
| Wong's wheel model[8] | Rigid wheel | Equations | 1D | Not applicable (n/a) | n/a | No | 1D |
| Wong's track model[9] | Track | Equations | 2D | Isotropic shear model | Ignored | No | 2D |
| MIT's model[23] | Rigid wheel | Equations | 1D | n/a | n/a | No | Closed-form solution |
| HIT's model[21,22] | Rigid wheel | Equations | 1D | n/a | n/a | Yes | 1D |
| Tran's model*[10,11] | Rigid wheel | Equations | 2D | Homogeneous soil assumption | Ignored | No | 2D |
| Tohoku UNIV's model[12,13] | Rigid wheel | Equations | 2D/3D | Linear motion approximation; Anisotropic shear model | Yes (Hegedus's formula) | No | 1D |
| AS$^2$ TM[15,16] | Elastic tire | S-function | 3D | Elastic-tire–soft-soil model from literatures | Not mentioned | Model the tire profile | Not mentioned |
| WTIM | Rigid wheel | *Matlab* function; S-function | 3D | Isotropic and anisotropic shear models both available | Yes (Bekker's formula) | Yes | 2D |

* Tran's model is actually a vehicle–soil model of a specific UGV based on a nonmodular approach.

wheel performance, was not theoretically studied in the model.

In fact, modeling of the lugged wheel (wheel with grousers) has rarely been studied in previous wheel–terrain interaction models. One exception is the wheel–soil model proposed in refs. [21, 22] for linear motion scenarios (referred to as HIT's model in subsequent sections). Unlike Wong's wheel model, where the normal and shear forces are distributed along a cylindrical surface determined by the wheel radius, the normal pressure and the shear stress in HIT's model are assumed to be along surfaces with radii equal to the wheel radius and the shear radius (a newly introduced variable defined as a function of the wheel radius and the lug height), respectively. Parameter tuning of soil physical properties is observed in ref. [22] to fit this model to the experiment results.

In ref. [23], researchers from MIT proposed a wheel–soil model for straight-line motion (referred to as MIT's model in following sections). Closed-form solutions for the drawbar pull and the driving torque were derived by linearizing the stresses along the wheel–soil interface, making real-time computation and on-line terrain parameter estimation possible.[23] However, this wheel–soil model only covers the linear motion maneuvers. A wheeled locomotion model appropriate for a variety of circumstances (such as the steering maneuvers) is required for the simulation of mobile robots.

An elastic-tire-and-soft-soil model $AS^2TM$ was developed by *AESCO*[16] for the prototyping and simulation of industrial off-road vehicles. This tire–soil model, which is mainly based on the research summarized in refs. [14, 15], can be used for off-road vehicle simulation in 3D environments, if combined with an auxiliary road module and a MBS dynamics solver. Unfortunately, the rigid wheel model, which is necessary for many robotic vehicles, is not available in the commercial version.[16] Nevertheless, this tire–soil model has been used to investigate rigid wheel performance by some researchers.[17] In addition, the relatively expensive cost limits further application of this commercial product.

A modular software package for the wheel–soil interaction is useful if it can be integrated either with a MBS dynamics solver or with vehicle dynamic equations to simulate different off-road vehicles and robots. The model we developed, called the "wheel terrain interaction model (WTIM)," incorporates many key concepts from previous studies of terramechanics. Our model was developed for the purpose of both dynamic simulations of mobile robots and the energy/power system design. A key future application of the WTIM package is the sizing of on-board power devices (batteries, motors, etc.) for mobile robots.

Table I gives a detailed comparison between WTIM and existing wheel/track/vehicle–terrain interaction models from the literature. The main contributions of WTIM are as follows:

(a) WTIM has been implemented as an open-source software package in the form of an *S-function*; its compatibility with MBS solvers and the modular, drag-and-drop features enable efficient tool-based simulation of mobile robots.
(b) WTIM uses improved approaches to calculate the stresses along the wheel–soil interface by including the influence of the wheel profiles (grousers) and the bulldozing effect contributed by the side surfaces during a steering maneuver.
(c) Parameter tuning of soil physical properties to fit wheel–soil models to the experiment results, which is observed in refs. [13, 22], can be avoided by using WTIM.

The remainder of this paper is organized as follows. The overall model architecture by incorporating WTIM with

https://doi.org/10.1017/S0263574711000798 Published online by Cambridge University Press

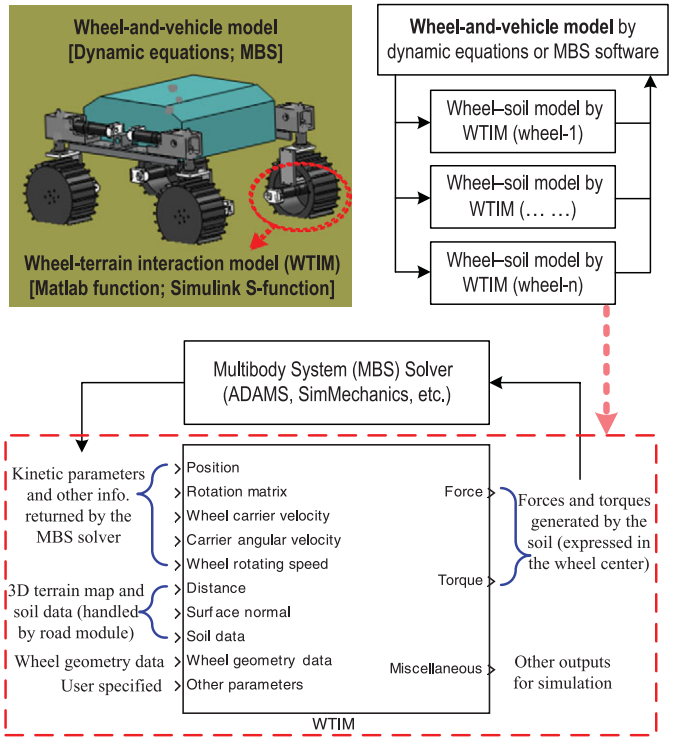


Fig. 1. (Colour online) Overall model architecture by integrating WTIM with the MBS software (or dynamic equations) to simulate mobile robots.

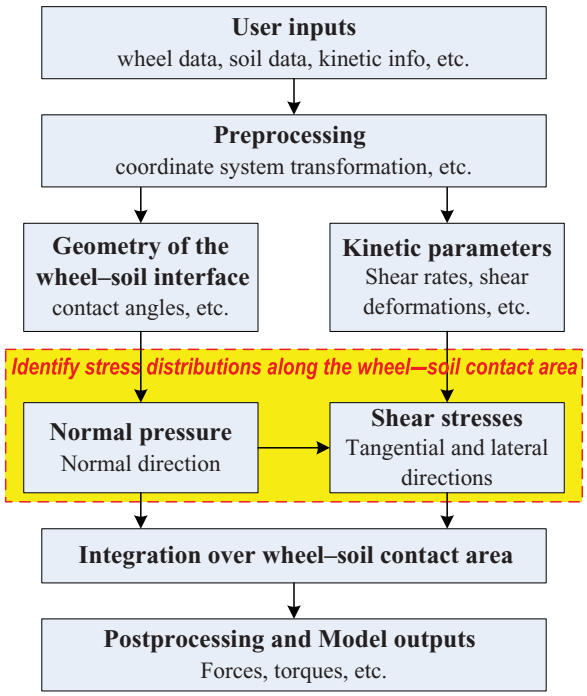


Fig. 2. (Colour online) General procedure for the wheel–terrain interaction modeling. The key task is to identify the stress distributions along the wheel–soil contact area based on knowledge of terramechanics.

the MBS software for simulation study is introduced in Section 2. Section 3 gives a detailed description of the wheel–terrain interaction modeling, with emphases on modeling the steering maneuvers and the influence of grousers. Simulation studies and experimental verifications of the proposed model are given in Section 4. Section 5 concludes the present paper.

## 2. Overall Model Architecture

Figure 1 shows the overall model architecture by integrating the WTIM package with the MBS software for off-road vehicle simulation. The wheel–soil interaction for each wheel of the robot is handled by a WTIM block while the overall robotic vehicle configuration is modeled by MBS software, such as *ADAMS* and *SimMechanics*. For each WTIM block, there are four groups of inputs (1) kinetic parameters and some other information captured by the MBS solver; (2) the 3D terrain geometry and the soil data, which are handled by an auxiliary road module; (3) the wheel geometry data; and (4) some other user-specified parameters for simulation study. The outputs of the WTIM block include the following: (1) the forces and torques exerted on the wheel by the soil, which will be returned to the MBS solver; and (2) some other parameters which may be required for simulations (outputs from the miscellaneous port), such as the slip ratio. It should be pointed out that the configurations of the robots/vehicles can also be modeled by user-written dynamic equations rather than the MBS solver.

## 3. Wheel–Terrain Interaction Modeling

As shown in Fig. 2, the wheel–terrain interaction modeling generally involves the following steps: (1) preprocessing, such as coordinate system (CS) transformations; (2) identify the geometric parameters of the wheel–soil interface, such as wheel sinkage and contact angles; (3) determine the shear rates and the shear deformations; (4) identify the normal pressure and shear stresses along the wheel–soil contact area by using terramechanics; (5) determine the forces and torques by integrating the stress distributions over the wheel–soil contact region; (6) postprocessing and CS transformations to output the forces and torques in the world frame or the wheel carrier frame, according to the user's requirements.

### *3.1. Coordinate systems and transformations*

For a modular modeling approach, CS transformations are required to express the soil deformations and reaction forces in the same frame. To be clear, all the coordinate frames defined in this paper follow the right-hand rule and the SAE standard directions. As shown in Fig. 3, the world reference frame $\Sigma_0$ is defined in the way such that the $x_0$-axis points to the north direction and the $z_0$-axis points vertically upward. Thus, the gravity force will be along the negative $z_0$-direction. A unit vector $N$ is used to represent the normal direction of the inclined surface and its coordinate in the world frame $\Sigma_0$ is

$$\mathbf{N} = [N^{x_0} \quad N^{y_0} \quad N^{z_0}]^{\mathrm{T}}. \tag{1}$$

We assume that the wheel carrier center and the wheel center coincide at point O. Frame $\Sigma_1$ is a CS attached to the wheel carrier with the $y_1$-axis coinciding with the rotation axis. The orientation between frame $\Sigma_1$ and frame $\Sigma_0$, which is determined by the rotation matrix $R_1^0$, can be calculated by the MBS solver. The coordinates of the wheel carrier center, and the translational and angular velocities of the

https://doi.org/10.1017/S0263574711000798 Published online by Cambridge University Press

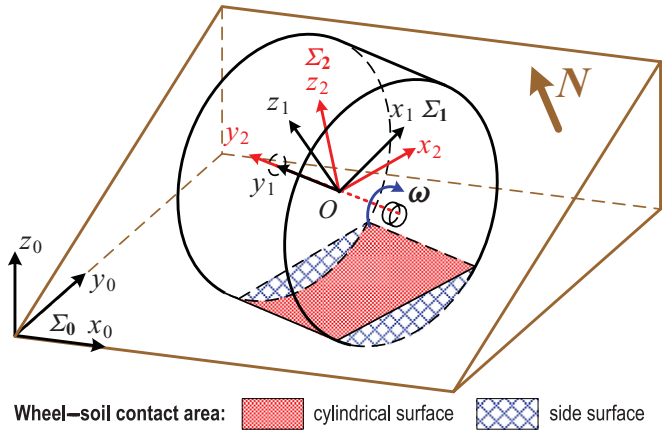


Fig. 3. (Colour online) A rigid wheel traveling on an inclined slope with the surface normal vector $N$. The wheel–soil contact area consists of a cylindrical surface and two side surfaces (if applicable).

wheel carrier can be expressed in the world frame $\Sigma_0$ as

$$\begin{cases} \mathbf{P}^{\mathbf{0}}_{\mathbf{wc}} = \begin{bmatrix} x_o^{x_0} & y_o^{y_0} & z_o^{z_0} \end{bmatrix}^{\mathrm{T}}, \\ \mathbf{v}^{\mathbf{0}}_{\mathbf{wc}} = \begin{bmatrix} v_o^{x_0} & v_o^{y_0} & v_o^{z_0} \end{bmatrix}^{\mathrm{T}}, \\ \Omega^{\mathbf{0}}_{\mathbf{wc}} = \begin{bmatrix} \Omega_o^{x_0} & \Omega_o^{y_0} & \Omega_o^{z_0} \end{bmatrix}^{\mathrm{T}}. \end{cases} \tag{2}$$

If the wheel travels over a flat surface, the $x_1$-axis will be parallel to the flat surface. Moreover, it will coincide with the longitudinal direction during linear motion scenarios. However, for many off-road vehicles and planetary exploration rovers, where the wheel carriers are connected to a suspension system or some articulated arms, the $x_1$-axis will no longer be parallel to the soil surface. For this purpose, a reference frame $\Sigma_2$ is introduced, with the $x_2$-axis parallel to the surface and the $y_2$-axis coinciding with the wheel rotating axis. In fact, $\Sigma_2$ and $\Sigma_1$ are related through a rotation about the $y_1$-axis by an angle $\theta_y$, which can be calculated by

$$\theta_y = -\sin^{-1}(N^{x_1}), \tag{3}$$

where $N^{x_1}$ is the $x_1$-component of $N$ in $\Sigma_1$. Then, the rotation matrix between $\Sigma_2$ and $\Sigma_1$ can be obtained as[18]

$$R_2^1 = \begin{bmatrix} \cos\theta_y & 0 & \sin\theta_y \\ 0 & 1 & 0 \\ -\sin\theta_y & 0 & \cos\theta_y \end{bmatrix}. \tag{4}$$

The translational and angular velocities of the wheel carrier can then be expressed in the reference frame $\Sigma_2$ as

$$\begin{cases} \mathbf{v}^{\mathbf{2}}_{\mathbf{wc}} = R_0^2 \mathbf{v}^{\mathbf{0}}_{\mathbf{wc}} = R_1^2 R_0^1 \mathbf{v}^{\mathbf{0}}_{\mathbf{wc}} = [v_x \quad v_y \quad v_z\,]^{\mathrm{T}}, \\ \Omega^{\mathbf{2}}_{\mathbf{wc}} = R_0^2 \Omega^{\mathbf{0}}_{\mathbf{wc}} = R_1^2 R_0^1 \Omega^{\mathbf{0}}_{\mathbf{wc}} = [\Omega_x \quad \Omega_y \quad \Omega_z\,]^{\mathrm{T}}. \end{cases} \tag{5}$$

It is important to make sure that

$$v_x \geq 0. \tag{6}$$

If this is not the case, a further rotation of 180° about the $z_2$-axis will be needed because only the forward motion has been modeled in the terramechanics model. Then, the velocity of the wheel center and the angular velocity of the rigid wheel can be obtained in the reference frame $\Sigma_2$ as

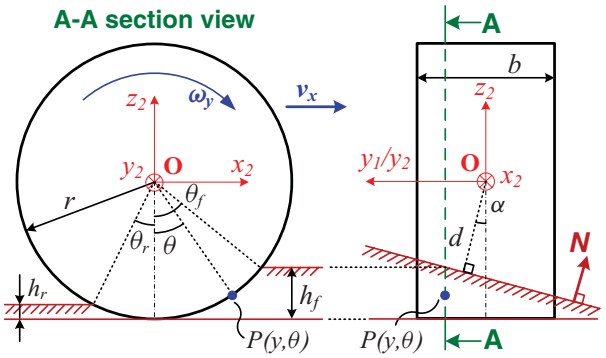


Fig. 4. (Colour online) Rear and side views of a rigid wheel on soft soil. $P(y,\theta)$ is a point on the cylindrical surface with contact angle equals to $\theta$.

$$\begin{cases} \mathbf{v} = \mathbf{v}^{\mathbf{2}}_{\mathbf{wc}} = [v_x \quad v_y \quad v_z]^{\mathrm{T}}, \\ \omega = [\Omega_x \quad \Omega_y + \omega \quad \Omega_z]^{\mathrm{T}} = [\omega_x \quad \omega_y \quad \omega_z]^{\mathrm{T}}, \end{cases} \tag{7}$$

where $\omega$ is the wheel rotational speed relative to the wheel carrier. All the subsequent derivations can be conducted in the reference frame $\Sigma_2$ after the above transformations.

### 3.2. *Geometry of the wheel–soil interface*

All the terramechanics models for the wheel–soil interaction are based on two fundamental relations, the pressure–sinkage relation and the shear–tension–displacement relation,[16] which can be experimentally identified by tests given in ref. [6]. The shear stress is a function of shear displacement and normal pressure, the latter of which can usually be determined by the geometry of the wheel–soil interface[1] based on terramechanics. Thus, we first identify the wheel sinkage and contact angles for the normal pressure in this section and then calculate the shear deformations for the shear stress in the next section.

Figure 4 shows two section views of the wheel–soil contact scenario given in Fig. 3. The distance from the wheel center to the ground surface $d$ can be identified by the road module. Let $\alpha$ ($\alpha$ is negative in Fig. 4) denote the angle between the $z_2$-axis and the ground surface normal vector $N$. Then,

$$\alpha = \sin^{-1}(N^{y_2}). \tag{8}$$

We consider a point $P(y, \theta)$ in the cylindrical wheel–soil interface, whose coordinate in frame $\Sigma_2$ can be expressed as

$$\mathbf{P}(y, \theta) = [r\sin\theta \quad y \quad -r\cos\theta\,]^{\mathrm{T}}. \tag{9}$$

In Fig. 4, $h_f(y)$ represents the wheel sinkage relative to the uncompacted soil in front of the wheel and $h_r(y)$ represents the rut recovery, as described in refs. [12, 16]. Let $\theta_f(y)$ and

[1] In the literatures, the term 'wheel-soil interface' usually refers to the cylindrical wheel-soil contact area, as shown in Fig. 3. Following this tradition, if not specially pointed out, the term 'wheel-soil interface' indicates the cylindrical wheel-soil contact region in this paper.

https://doi.org/10.1017/S0263574711000798 Published online by Cambridge University Press

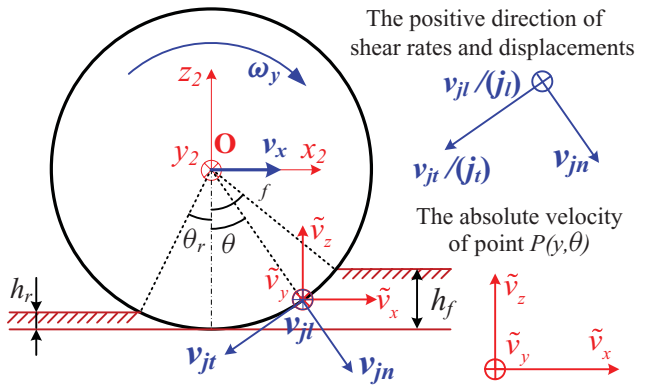


Fig. 5. (Colour online) Determination of the shear rates corresponding to point $P(y,\theta)$ at the wheel–soil interface (cylindrical surface).

$\theta_r(y)$ denote the corresponding entry contact angle and the exit angle, respectively. From Fig. 4, we have

$$\begin{aligned} h_f(y) &= r - d/\cos\alpha - y\tan\alpha, \\ &= r - d\Big/\sqrt{1-(N^{y_2})^2} - y\cdot N^{y_2}\Big/\sqrt{1-(N^{y_2})^2}, \end{aligned} \tag{10}$$

$$\theta_f(y) = \cos^{-1}(1 - h_f(y)/r), \tag{11}$$

$$\theta_r(y) = -\cos^{-1}(1 - \lambda\cdot h_f(y)/r), \tag{12}$$

where $\lambda$ is the ratio between $h_r(y)$ and $h_f(y)$, which can be experimentally measured by sensing systems, e.g., a vision system.[12] Other formulas and techniques can also be used to identify $\lambda$ and $\theta_r(y)$.[16] In the later sections, we will give some of these alternative formulas.

### 3.3. Shear rates and shear deformations

As shown in Fig. 5, the absolute velocity of point $P(y, \theta)$ relative to the world frame can be expressed in frame $\Sigma_2$ as

$$\mathbf{v}(y,\theta) = \begin{bmatrix} \tilde{v}_x \\ \tilde{v}_y \\ \tilde{v}_z \end{bmatrix} = \begin{bmatrix} v_x - \omega_z y - \omega_y r\cos\theta \\ v_y + \omega_z r\sin\theta + \omega_x r\cos\theta \\ v_z - \omega_y r\sin\theta + \omega_x y \end{bmatrix}. \tag{13}$$

By decomposing this velocity into the tangential, lateral, and normal directions (Fig. 5), the tangential shear rate $v_{jt}$, the lateral shear rate $v_{jl}$, and the compression speed $v_{jn}$ (the positive directions of these speeds are given in Fig. 5) can be derived as

$$\begin{aligned} v_{jt}(y,\theta) &= -\tilde{v}_z\sin\theta - \tilde{v}_x\cos\theta, \\ &= -(v_z + \omega_x y)\sin\theta - (v_x - \omega_z y)\cos\theta + \omega_y r, \\ v_{jl}(y,\theta) &= \tilde{v}_y = v_y + \omega_z r\sin\theta + \omega_x r\cos\theta, \\ v_{jn}(y,\theta) &= \tilde{v}_x\sin\theta - \tilde{v}_z\cos\theta, \\ &= (v_x - \omega_z y)\sin\theta - (v_z + \omega_x y)\cos\theta. \end{aligned} \tag{14}$$

By following the approach in ref. [8], shear deformations of the point $P(y, \theta)$ on the wheel–soil interface can be determined by integrating the corresponding shear rates from the entry position when this point makes the first contact with the soil to its current position. By assuming that $v_x$, $v_y$, $v_z$, $\omega_x$, $\omega_y$, and $\omega_z$ are slowly time-varying and hence can be approximated as constants during the short time interval of the integration, the shear deformations (the positive directions are given in Fig. 5) along the tangential and lateral directions are

$$\begin{aligned} j_t(y,\theta) &= \begin{bmatrix} (-v_x + \omega_z y)(s\theta_f - s\theta) + (v_z + \omega_x y) \\ \cdot(c\theta_f - c\theta) + \omega_y r(\theta_f - \theta) \end{bmatrix}\Big/\omega_y, \\ j_l(y,\theta) &= \begin{bmatrix} v_y(\theta_f - \theta) + \omega_z r(c\theta - c\theta_f) \\ + \omega_x r(s\theta_f - s\theta) \end{bmatrix}\Big/\omega_y, \end{aligned} \tag{15}$$

where $s\theta \equiv \sin\theta$, $c\theta \equiv \cos\theta$, and $\omega_y \neq 0$.

In ref. [19], the authors considered the time-varying case for a tracked robot and proposed an alternative method to identify the shear deformations by solving partial differential equations. This approach may be modified and applied to wheeled robots. However, it is expected to be much more complex because the wheel–soil interface is a cylindrical surface and the entry angle of the wheel is time-varying, whereas for a tracked vehicle the entire track is assumed to remain in contact with the flat soil.[19] Moreover, wheel–soil interaction models based on quasi-static approaches are in reasonably close agreement with experiment results as seen in refs. [8–13]. Therefore, we use a quasi-static approach in WTIM.

### 3.4. Stress distributions along the wheel–soil interface

Wong's formulas given in ref. [8] are extended to compute the normal and the shear stress distributions along the wheel–soil interface. The normal stress can be formulated as

$$\sigma(y,\theta) = \begin{cases} C_\sigma[\cos\theta - \cos\theta_f(y)]^n & (\theta_m(y) \le \theta \le \theta_f(y)), \\ C_\sigma[\cos\theta_{eq}(y) - \cos\theta_f(y)]^n & (\theta_r(y) \le \theta < \theta_m(y)), \end{cases} \tag{16}$$

where $C_\sigma$ is a constant parameter and $\theta_{eq}(y)$ is the equivalent front region contact angle for points in the rear region. They can be determined as

$$C_\sigma = \begin{cases} r^n(k_c/b + k_\phi) & (\text{by Bekker's formula}), \\ (r/b)^n(ck_c' + \gamma bk_\phi') & (\text{by Reece's formula}), \end{cases} \tag{17}$$

$$\theta_{eq}(y) = \theta_f(y) - \frac{\theta - \theta_r(y)}{\theta_m(y) - \theta_r(y)}\cdot(\theta_f(y) - \theta_m(y)). \tag{18}$$

In addition, $\theta_m(y)$ is the contact angle corresponding to the maximal normal stress and can be obtained as

$$\theta_m(y) = (a_0 + a_1\cdot s)\theta_f(y), \tag{19}$$

where $a_0$ and $a_1$ are constant parameters defined in ref. [8] and their values will depend on the wheel–soil interactions. The parameter $s$ is the slip ratio, which can be expressed as

$$s = \begin{cases} (\omega_y r - v_x)/(\omega_y r) & (|\omega_y r| > |v_x|), \\ (\omega_y r - v_x)/v_x & (|\omega_y r| < |v_x|). \end{cases} \tag{20}$$

In the wheel–soil model for the steering maneuver given in ref. [12], the shear stress along the wheel–soil interface

https://doi.org/10.1017/S0263574711000798 Published online by Cambridge University Press

was assumed to be anisotropic. Two new variables, defined as the tangential and the lateral shear modulus, are introduced to calculate the shear stresses along the tangential and the lateral directions, respectively. It is uncertain, however, that this method is generally applicable. Moreover, only the traditional shear modulus, as defined in ref. [6], can be experimentally measured by terramechanics shear tests. A method to measure the tangential and the lateral shear modulus, if possible, is not available in literature.

Just like the modeling of the track–soil interaction in ref. [9], isotropic modeling of the shear stress distributions during a turning maneuver is expected to be a better choice over the anisotropic method for wheeled robotic vehicles. Two basic assumptions for this isotropic modeling are:

(1) The magnitude of the shear stress developed at a certain point along the wheel–soil interface is a function of the overall shear displacement at that point, as described by the shear–stress–displacement formulas given in ref. [6].
(2) The direction of the shear stress at a point on the wheel–soil interface is opposite to that of the shearing velocity of the wheel with respect to the ground at that point.

Analogous[2] to the case for the track–soil model given in ref. [9], the overall shear displacement of point $P(y,\theta)$ with respect to the soil can be computed as

$$j(y,\theta) = \sqrt{j_t(y,\theta)^2 + j_l(y,\theta)^2}. \tag{21}$$

Using the shear formula given by Janosi and Hanamoto,[6] the magnitude of the shear stress can be computed as

$$\tau(y,\theta) = \tau_{\max} \cdot [1 - \exp(-|j(y,\theta)|/K)], \tag{22}$$

$$\tau_{\max} = c + \sigma(y,\theta) \cdot \tan\phi, \tag{23}$$

where $\tau_{\max}$ is the maximal shear stress corresponding to the normal pressure $\sigma(y, \theta)$, $c$ that represents the cohesion of the soil, and $\phi$ is the internal friction angle of the soil.

For certain muskegs, dry sands, and certain snows, where the shear curve exhibits a "hump" of maximum shear stress and then decreases continuously with the increase of the shear deformation, Wong's shear formula[6] should be used

$$\tau(y,\theta) = \tau_{\max} K_r [1 - \exp(-j(y,\theta)/K_w)] \times [1 + [1/(K_r(1 - e^{-1}) - 1)] \exp(1 - j(y,\theta)/K_w)], \tag{24}$$

where $K_r$ is the residual shear stress to $\tau_{\max}$, and $K_w$ is the corresponding shear deformation where $\tau_{\max}$ occurs.

The tangential and the lateral shear stresses (the positive directions are given in Fig. 6) can be obtained as

$$\tau_t(y,\theta) = \tau(y,\theta) \cdot \frac{v_{jt}(y,\theta)}{\sqrt{v_{jt}(y,\theta)^2 + v_{jl}(y,\theta)^2}},$$
$$\tau_l(y,\theta) = \tau(y,\theta) \cdot \frac{v_{jl}(y,\theta)}{\sqrt{v_{jt}(y,\theta)^2 + v_{jl}(y,\theta)^2}}. \tag{25}$$

[2] This wheel-and-track analogy (the cylindrical wheel-soil interface is analogous to the planar track-soil interface) method has been used to identify the soil deformation along the wheel-soil interface in linear motion scenarios, as shown in ref. [8].

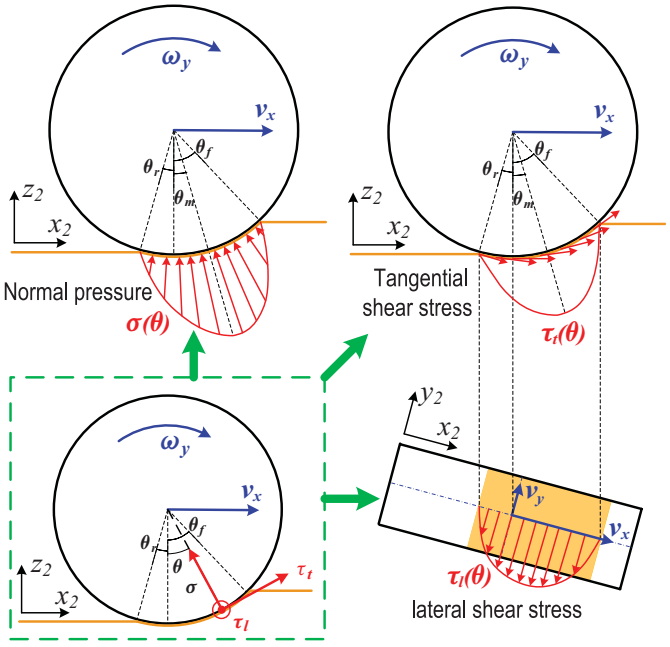


Fig. 6. (Colour online) The normal and shear stress distributions along the wheel–soil interface (cylindrical surface).

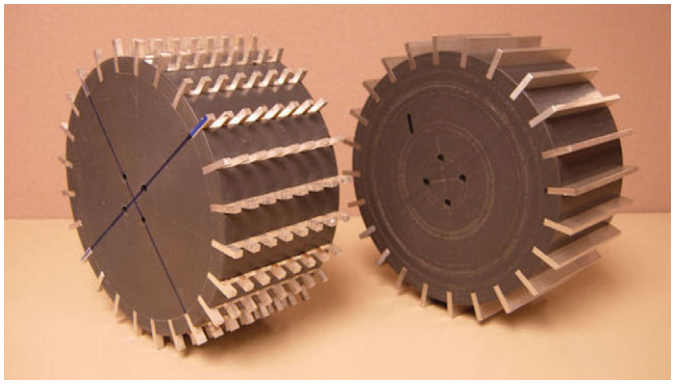

Fig. 7. (Colour online) Typical lugged wheels for mobile robots.

For complete purposes, anisotropic shear stress formulas corresponding to Eqs. (22) and (24) are also included

$$\tau_i(y,\theta) = \operatorname{sgn}(j_i(y,\theta)) \cdot \tau_{\max} \cdot [1 - \exp(-|j_i(y,\theta)|/K_i)] \ (i = t, l), \tag{26}$$

$$\tau_i(y,\theta) = \left[1 + \frac{1}{K_{ri}(1 - e^{-1}) - 1} \exp(1 - j_i(y,\theta)/K_{wi})\right] \times K_{ri}[1 - \exp(-j_i(y,\theta)/K_{wi})]\tau_{\max} \ (i = t, l), \tag{27}$$

where $K_t$ and $K_l$ are the tangential and lateral shear stress modulus of the soil, respectively, as defined in ref. [12]; $K_{ri}$ and $K_{wi}$ are defined as variables analogously to $K_r$ and $K_w$ in Eq. (24) for the tangential and lateral directions, respectively.

### 3.5. *Consider the influence of grousers*

Purely smooth wheels are rarely used in real applications. Instead, to improve the traction performance, many wheels are equipped with certain profiles or grousers, as shown in Fig. 7. For simplifications, the lugged wheels are usually

https://doi.org/10.1017/S0263574711000798 Published online by Cambridge University Press

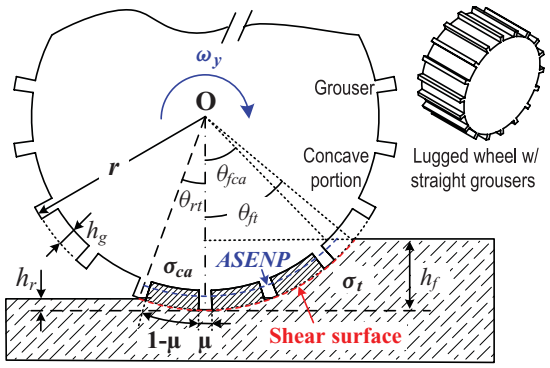


Fig. 8. (Colour online) The model of a driven lugged wheel on soft soil. If the area ratio $\mu$ is small, the equivalent normal pressure can be approximated by the pressure along the approximated surface of equivalent normal pressure (ASENP), which is close to the concave portion. The shear phenomenon takes place along the shear surface across the grouser tips.[6] Modeling of the lugs/grousers will be required if the distance between the ASENP and the shear surface cannot be neglected compared to wheel sinkage.

modeled as smooth wheels, which we call smooth wheel approximation in this paper. In ref. [12], by tuning soil parameters, such as the shear modulus, which usually dominates the shear stress and the wheel performance, simulation results by the smooth wheel approximation method are considered to be in close agreement with experiment data for lugged wheels. This parameter tuning method, however, is not as sound as it appears, since the shear modulus is originally defined as a constant parameter to represent the inherent property of the soil. Its value should be measured by shear test experiment[6] and will be constant once the soil is given. Additionally, the experiment results in ref. [20] indicate that the influence of grousers cannot be neglected for lugged wheels, which are usually used by robotic planetary rovers. Thus, modeling of lugged wheels is required for more reasonable and reliable simulation results.

A typical lugged wheel usually consists of two portions as shown in Fig. 8: the grousers and the concave portion. In Fig. 8, $r$ is defined to be the radius of the bigger circle surrounding the grouser tip, $h_g$ is the grouser height, and $\mu$ is the area ratio of the grouser tip. Let $\theta_{ft}$ and $\theta_{fca}$ denote the entry contact angles corresponding to the grouser tip and the concave portion, respectively. From the geometric relations, we have

$$\theta_{ft}(y) = \cos^{-1}(1 - h_f(y)/r), \tag{28}$$

$$\theta_{fca}(y) = \begin{cases} \cos^{-1}(r - h_f(y)/(r - h_g)) & (h_f(y) > h_g) \\ 0 & (\text{otherwise}). \end{cases} \tag{29}$$

We assume that the effective exit angle of the grouser tip equals that of the concave portion. Then, we have

$$\theta_{rt}(y) = \theta_{rca}(y) = \theta_r(y) = -\cos^{-1}(1 - \lambda \cdot h_f(y)/r). \tag{30}$$

Instead of measuring the ratio $\lambda$ by a vision system,[12] an alternative analytical formula for this parameter is required for simulation. By considering the rut recovery and the soil transported by the grousers, such a formula can be given as

$$\lambda = (\lambda_0 + \lambda_1 s)(k_c/b + k_\phi)(r - d)^{n-1}/k_\phi, \tag{31}$$

where $\lambda_0$ and $\lambda_1$ are two constant parameters.
Analogous to the formula given in Eq. (19), an alternative formula for the exit angles can be expressed as

$$\theta_r(y) = (b_0 + b_1 s)\theta_{ft}(y). \tag{32}$$

The stresses can be determined based on two assumptions[3] (1) the equivalent normal stress $\sigma_e$ is assumed to be the average value of the normal stresses at the grouser tip portion and the concave portion; (2) the shear phenomenon between the wheel and the soil is assumed to take place along a cylindrical surface determined by the shear radius, which usually equals the radius of the grouser tips. Then, the equivalent normal stress $\sigma_e$ is

$$\sigma_e(y,\theta) = \begin{cases} \mu\sigma_t(y,\theta) + (1-\mu)\sigma_{ca}(y,\theta) & (\theta_r(y) \le \theta \le \theta_{fca}(y)) \\ \mu\sigma_t(y,\theta) & (\theta_{fca}(y) \le \theta \le \theta_{ft}(y)). \end{cases} \tag{33}$$

By substituting the equivalent normal pressure $\sigma_e(y,\theta)$ into Eq. (23), the equivalent shear stresses $\tau_{et}(y,\theta)$ and $\tau_{el}(y,\theta)$ can then be derived by Eqs. (25)–(27).

### *3.6. Forces and torques by the soil*

The forces and torques exerted on the wheel by the soil can be determined by integrating the distributed stresses along the wheel–soil interface. The components of stresses along the cylindrical contact region can be determined in frame $\Sigma_2$ as

$$\begin{cases} \sigma_x(y,\theta) = -\sigma_e(y,\theta)s\theta & \tau_x(y,\theta) = \tau_{et}(y,\theta)c\theta \\ \sigma_y(y,\theta) = 0 & \tau_y(y,\theta) = -\tau_{el}(y,\theta) \\ \sigma_z(y,\theta) = \sigma_e(y,\theta)c\theta & \tau_z(y,\theta) = \tau_{et}(y,\theta)s\theta \end{cases} \tag{34}$$
$(s\theta \equiv \sin\theta, c\theta \equiv \cos\theta).$

By integrating these components with respect to an area increment $r\mathrm{d}\theta\mathrm{d}y$ along the cylindrical wheel–soil interface, the forces exerted on the wheel can be determined as

$$\begin{cases} F_x = \displaystyle\int_{-b/2}^{b/2}\int_{\theta_r(y)}^{\theta_f(y)} r(-\sigma_e(y,\theta)s\theta + \tau_{et}(y,\theta)c\theta)\,\mathrm{d}\theta\,\mathrm{d}y \\ F_y = -\displaystyle\int_{-b/2}^{b/2}\int_{\theta_r(y)}^{\theta_f(y)} r\cdot\tau_{el}(y,\theta)\,\mathrm{d}\theta\,\mathrm{d}y \\ F_z = \displaystyle\int_{-b/2}^{b/2}\int_{\theta_r(y)}^{\theta_f(y)} r(\sigma_e(y,\theta)c\theta + \tau_{et}(y,\theta)s\theta)\,\mathrm{d}\theta\,\mathrm{d}y. \end{cases} \tag{35}$$

[3] Based on these assumptions, other types of lugs/grousers, such as the zigzag wheel pattern used by Mars Science Laboratory, can be modeled as straight grousers (Fig. 8) with the same area ratio $\mu$ and lug height $h_g$. Therefore, the grouser modeling method proposed in this paper is expected to work for a wide variety of wheel profiles. It should be pointed out that only the average effect of the grousers is modeled while the fluctuations of forces and torques observed in the experiments in refs. [3, 22] are neglected for simplification.

https://doi.org/10.1017/S0263574711000798 Published online by Cambridge University Press

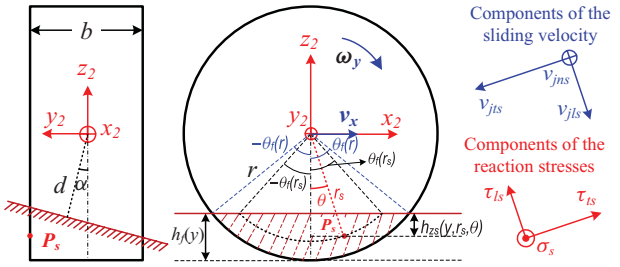


Fig. 9. (Colour online) Modeling the stresses contributed by the side surfaces.

The corresponding torques can be computed as

$$\begin{cases} M_x = \int y\mathrm{d}F_z - \int (-r\cos\theta)\mathrm{d}F_y \\ \quad = \int_{-b/2}^{b/2}\int_{\theta_r(y)}^{\theta_f(y)} \begin{bmatrix} ry\sigma_e(y,\theta)c\theta + \\ ry\tau_{et}(y,\theta)s\theta - r^2\tau_{el}(y,\theta)c\theta \end{bmatrix} \mathrm{d}\theta\ \mathrm{d}y \\ M_y = \int (-r\cos\theta)\mathrm{d}F_x - \int (r\sin\theta)\mathrm{d}F_z \\ \quad = -r^2\int_{-b/2}^{b/2}\int_{\theta_r(y)}^{\theta_f(y)} \tau_{et}(y,\theta)\mathrm{d}\theta\mathrm{d}y \\ M_z = \int (r\sin\theta)\mathrm{d}F_y - \int y\mathrm{d}F_x \\ \quad = \int_{-b/2}^{b/2}\int_{\theta_r(y)}^{\theta_f(y)} \begin{bmatrix} ry\sigma_e(y,\theta)s\theta - \\ ry\tau_{et}(y,\theta)c\theta - r^2\tau_{el}(y,\theta)s\theta \end{bmatrix} \mathrm{d}\theta\ \mathrm{d}y. \end{cases} \tag{36}$$

Numerical methods, such as the composite Simpson's rule and high-order Gaussian quadrature method, are used in WTIM to evaluate these two-dimensional integrals. These forces and torques can then be transformed into the world coordinate or the wheel carrier frame through the corresponding rotation matrices discussed in Section 3.1.

### *3.7. Contribution of the side surfaces*

For rigid wheels with sidewalls, the bulldozing effect of the side surfaces may make considerable contribution to the lateral force during a steering maneuver. In ref. [12], the bulldozing resistance due to the side surface is estimated by Hegedus's method for the case where the surcharge reached the saturation state. Moments due to the side surface are not modeled, since the pressure formula corresponding to the saturation state is not yet available. In addition, the modeling of side surface in ref. [12] only covers very limited scenarios. In the following, we model the case where the wheel just begins to cause soil failure and the surcharge has not been developed.

As shown in Fig. 9, the coordinate of the point $P_s$ in the side surface can be expressed in frame $\Sigma_2$ as

$$\mathbf{P_s}(y, r_s, \theta) = [r_s\sin\theta,\ y,\ -r_s\cos\theta]^{\mathrm{T}} \quad (y = \pm b/2), \tag{37}$$

where $r_s$ is the distance from point $P_s$ to the wheel center. The corresponding shear rates and displacements for point $P_s$ can be derived in a manner similar to Section 3.3. Notice that the normal pressure can only be generated when the wheel's side surface compresses the soil. Then, based on the formula for the bulldozing effect of plates given in ref. [4], we have

$$\sigma_s(y, r_s, \theta) = \mathrm{sgn}(y)\begin{pmatrix} 2c\tan(45^\circ + \phi/2) + \gamma Z^{z_2}\cdot \\ \tan(45^\circ + \phi/2)^2 h_{zs}(y, r_s, \theta) \end{pmatrix}, \quad \left(\begin{cases} y = \pm b/2 & \text{(only in the side surfaces)} \\ y\cdot v_{jns} > 0 & \text{(wheel compresses the soil)} \end{cases}\right), \tag{38}$$

where $\gamma$ is the density of the soil, $Z^{z_2}$ is the projection of the world $z_0$-axis onto the $z_2$-axis in $\Sigma_2$, $h_{zs}$ is the corresponding underground depth along the $z_2$-axis and can be obtained as

$$h_{zs}(y, r_s, \theta) = r_s\cos\theta + h_f(y) - r. \tag{39}$$

For lugged wheels, the normal pressure over the grouser portion region can be expressed as

$$\sigma_s(y, r_s, \theta) = \mu\cdot\mathrm{sgn}(y)\begin{pmatrix} 2c\tan(45^\circ + \phi/2) + \gamma Z^{z_2}\cdot \\ h_{zs}(y, r_s, \theta)\tan(45^\circ + \phi/2)^2 \end{pmatrix}, \quad (y = \pm b/2,\ y\cdot v_{jns} > 0,\ r - h_g \le r_s \le r). \tag{40}$$

For a given point on the side surface, the shear stress can be developed only if the normal pressure exists at this point. Then, the shear stresses can be calculated in a way similar to Section 3.4, with the maximum shear stress expressed as

$$\tau_{\max}(y, r_s, \theta) = \sigma_s(y, r_s, \theta)\tan\phi. \tag{41}$$

By integrating these distributed stresses with respect to an area increment $r_s d\theta dr_s$ along the contact region where

$$\begin{cases} r - h_f \le r_s \le r \\ -\cos^{-1}((r - h_f)/r_s) \le \theta \le \cos^{-1}((r - h_f)/r_s) \end{cases} \tag{42}$$

the forces and torques contributed by the side surface can be derived similarly to the process described in Section 3.6 and hence are not repeated.

## 4. Simulation and Experimental Verifications

WTIM has been realized as a *Simulink S-Function* (Fig. 1). The computationally intensive portion is written in *ANSI C* and compiled as an *MEX* file to speed up the simulation. Currently, a single step calculation costs about 16 ms at the *HP Z400* workstation with an *Intel Xeon 3520* CPU @ 2.66 GHz and 6 GB of RAM. In the following, we test the model by using field experiment data available in the literature.

### *4.1. Traction performance of lugged wheels*

In refs. [20, 22], single-wheel, linear motion experiments were conducted to investigate the effect of slip and grousers on the traction performance of rigid wheels for lunar/planetary rovers. Drawbar pull and the driving torque were measured for a range of slip ratios under a given wheel load. Meanwhile, physical properties of the soil (air-dried sand) used in the experiments were measured using standard terramechanics tests.[22] The soil parameters, the wheel geometric data, and other parameters required for the simulation are listed in Table II.

https://doi.org/10.1017/S0263574711000798 Published online by Cambridge University Press

Table II. Simulation parameters and values.

| Parameter | Value | Unit | Description |
|---|---|---|---|
| $\gamma$ | 15.729 | kN/m$^3$ | Soil density |
| $c$ | 0.251 | kPa | Cohesion |
| $\phi$ | 31.9 | deg | Internal friction angle |
| $n$ | 1.098 | – | Sinkage exponent |
| $k_c$ | 15.6 | kN/m$^{n+1}$ | Cohesive modulus |
| $k_\phi$ | 2407.4 | kN/m$^{n+2}$ | Frictional modulus |
| $K_r$ | 0.96 | – | Residual shear stress |
| $K_w$ | 0.018 | m | Modulus in Eq. (24) |
| $r_0$ | 0.135 | m | Radius (concave portion) |
| $b$ | 0.165 | m | Wheel width |
| $h_g$ | 5/10/15 | mm | Lug height of the grousers |
| $l_w$ | 1.5 | mm | The grouser thickness |
| $W_{load}$ | 80.0 | N | Wheel load |
| $a_0$ | 0.40 | – | Coefficient for $\theta_m$ |
| $a_1$ | 0.50 | – | Coefficient for $\theta_m$ |
| $b_0$ | −0.13 | – | Coefficient for $\theta_r$ |
| $b_1$ | 0.0 | – | Coefficient for $\theta_r$ |

The simulation procedure is summarized as (1) input data; (2) find the entry angle (or the wheel sinkage) corresponding to the wheel load by interpolation or binary search method; (3) compute the drawbar pull and driving torque based on the entry angle (or the wheel sinkage) acquired in step 2. Equation (32) is used to estimate the exit angles while Eq. (24) is used to calculate the shear stresses. The area ratio of the grouser tip is

$$\mu = l_w \cdot (360^\circ/15^\circ)/(2\pi(r_0 + h_g)). \tag{43}$$

It is observed that the height of grousers ($h_g$ in Fig. 8) has a significant influence on the wheels' traction performance, as shown in Fig. 10. The simulation results by WTIM agree well with the experiment results, especially when the slip ratio is in the range of [0.10, 0.60]. Thus, it seems the proposed model in WTIM can predict the linear motion performance of lugged wheels very well by noticing that the preferable range of the slip ratio in real application is from 10% to 45%.[20]

### *4.2. Single wheel experiments for steering maneuver*

In refs. [24, 25], the researchers from the Tohoku University investigated the steering performance of rigid wheels for the turning maneuver of planetary/lunar rovers. As shown in Fig. 11, both the smooth wheel (wheel-A) and the lugged wheel (wheel-B) were experimentally studied. The soil used in the experiments is the FJS-1 lunar regolith simulant,[24] an artificial soil, which is used to simulate the real lunar soil returned by *The Apollo Program*. Physical properties of this lunar regolith simulant are close to those of the real lunar soil and are given in Table III. The forces and torques generated during the wheel locomotion were measured by a six-axis Force/Torque sensor. By setting the slip ratio from 0.0 to 0.9, in steps of 0.1, and the steering angle (which is equal to the slip angle $\beta$) from 4° to 16°, in steps of 4°, the experiments were repeated at least twice under the aforementioned conditions.

A model, termed the reference model in this section, for the steering maneuver of smooth, rigid wheels was derived based

Table III. Simulation parameters and values for the soil.

| Parameter | Value | Unit | Description |
|---|---|---|---|
| $\gamma$ | 15.68 | kN/m$^3$ | Soil density |
| $c$ | 0.80 | kPa | Cohesion |
| $\phi$ | 37.2 | deg | Internal friction angle |
| $n$ | 1.0 | – | Sinkage exponent |
| $k_c$ | 1.37 | kN/m$^{n+1}$ | Cohesive modulus |
| $k_\phi$ | 814 | kN/m$^{n+2}$ | Frictional modulus |
| $K$ | 0.020 | m | Shear modulus of the soil |

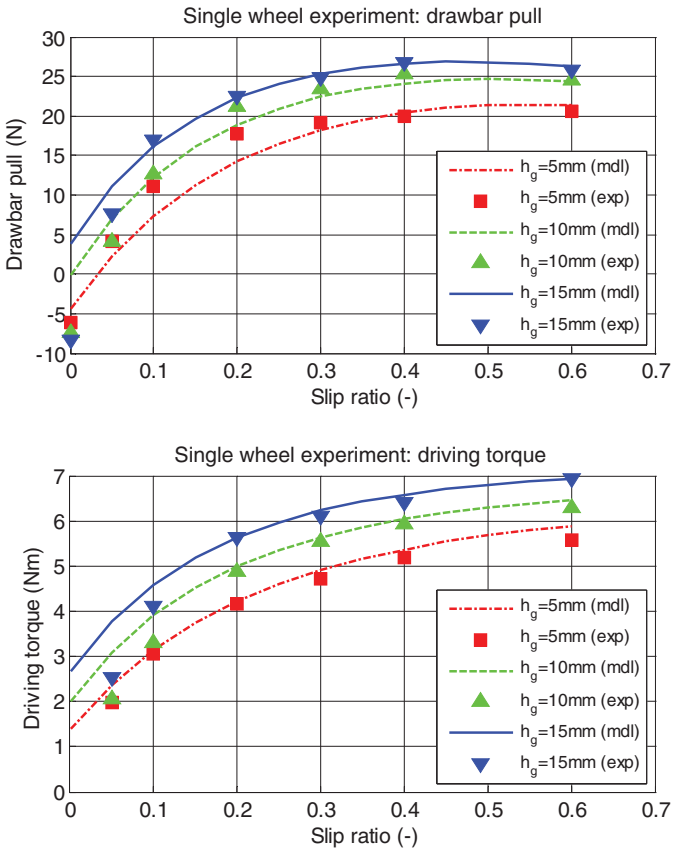


Fig. 10. (Colour online) Drawbar pull and driving torque for lugged wheels. The notations (sim) and (exp) represent the simulation results by WTIM and the experiment results, respectively.

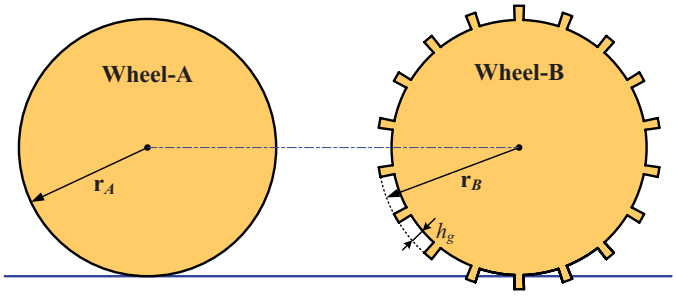


Fig. 11. (Colour online) Rigid wheels used in the experiments. From left to right: wheel without paddle (wheel-A), wheel with paddle (wheel-B).

https://doi.org/10.1017/S0263574711000798 Published online by Cambridge University Press

Table IV. Simulation parameters and values for wheel-A and wheel-B.

| Parameter | Wheel-A | Wheel-B | Unit | Description |
|---|---|---|---|---|
| $r$ | 0.092 | 0.100 | m | Shear radius |
| $b$ | 0.107 | 0.107 | m | Wheel width |
| $h_g$ | 0 | 0.008 | m | Grouser height |
| $\mu$ | 0 | 0.1146 | – | Grouser area ratio |
| $W_{load}$ | 64.68 | 64.68 | N | Wheel load |
| $a_0$ | 0.25 | 0.30 | – | Coef. for $\theta_m$ |
| $a_1$ | 0.50 | 0.32 | – | Coef. for $\theta_m$ |
| $b_0$ | −0.15 | −0.20 | – | Coef. for $\theta_r$ |
| $b_1$ | 0.0 | 0.0 | – | Coef. for $\theta_r$ |

on the anisotropic shear stress approach. In the reference model, rather than modeling the influence of grousers, the author used this "smooth wheel" model, with tuning of the shear moduli to fit the simulation results to the experiment results, as introduced in the sections above.

The isotropic shear stress approach is used by WTIM for simulation. Table IV lists some other inputs for WTIM, such as the wheel geometry data and the wheel load. The simulation procedure is similar to Section 4.1 and hence not repeated.

Figure 12 shows the experiment results, the simulation results by the reference model,[25] and the simulation results by WTIM. For a certain type of wheel, the drawbar pull increases with respect to the slip ratio due to the increasing shear deformation in the longitudinal direction. The lateral force decreases with respect to the slip ratio and increases with respect to the slip angle. The characteristics of the lateral force are a result of its close dependence on the lateral shear deformation, which also decreases with respect to the slip ratio and increases with respect to the slip angle. It is also observed that the surface patterns have a significant influence on the wheel performance. As shown in Fig. 12, the drawbar pull and the lateral force of the lugged wheel (wheel-B) are significantly bigger than those of the smooth wheel (wheel-A) under the same conditions. This is mainly due to relatively larger shear deformation, and thus greater shear stresses, developed by the lugged wheel under the same load as the smooth wheel.

Simulation results by WTIM are in better agreement[4] with the experimental data than those of the reference model. This is especially true for the lugged wheel (wheel-B), as shown in Fig. 12. To quantitatively evaluate the model goodness of fit, a new variable is introduced, as defined in Eq. (44), in analogy to the coefficient of determination for general data fitting

$$\mathrm{R-square(mdl)} = 1 - \frac{\sum_{s_i} (\exp(s_i) - \mathrm{mdl(s_i)})^2}{\sum_{s_i} \left(\exp(s_i) - \overline{\exp(\mathrm{s_i})}\right)^2} \quad (44)$$
$$\left( \begin{cases} \mathrm{mdl(s_i)} : \mathrm{model\ result @\ slip} = \mathrm{s_i} \\ \exp(\mathrm{s_i}) : \mathrm{experiment\ (meanvalue) @ slip} = \mathrm{s_i} \end{cases} \right).$$

[4] Relatively large differences between the simulation results and the experimental results are observed for the longitudinal drawbar pull at very large slip ratios. One possible reason is that the soil under the wheel becomes fluidized and different mechanics may dominate the phenomena at high slip ratios[12].

Table V. R-square[5] values for the reference model and WTIM.

| | Wheel-A | | Wheel-B | |
|---|---|---|---|---|
| R-square | Ref. model | WTIM | Ref. model | WTIM |
| $F_x(\beta = 4^\circ)$ | 0.5098 | 0.8510 | 0.4041 | 0.6773 |
| $F_y(\beta = 4^\circ)$ | 0.2452 | −0.0677 | 0.6445 | 0.5040 |
| $F_x(\beta = 8^\circ)$ | 0.6309 | 0.8427 | 0.4461 | 0.7454 |
| $F_y(\beta = 8^\circ)$ | 0.5861 | 0.8573 | 0.7058 | 0.9498 |
| $F_x(\beta = 12^\circ)$ | 0.6714 | 0.8654 | 0.5224 | 0.8370 |
| $F_y(\beta = 12^\circ)$ | 0.7054 | 0.9109 | 0.7374 | 0.9591 |
| $F_x(\beta = 16^\circ)$ | 0.8425 | 0.8011 | 0.4587 | 0.7991 |
| $F_y(\beta = 16^\circ)$ | 0.7033 | 0.8993 | 0.7401 | 0.9499 |
| *Mean* | **0.6118** | **0.7450** | **0.5824** | **0.8027** |

Under this definition, the "R-square" value of a given model approaches one as the model outputs become closer to the experimental results. The "R-square" values corresponding to the reference model and WTIM for wheel-A and wheel-B are listed in Table V. Despite tuning the shear modulus in the reference model to fit each experiment, WTIM still gives better simulation results in a general sense. A 21.8% improvement of the mean "R-square" value by WTIM compared to the reference model has been achieved for the smooth wheel (wheel-A). The reason is that WTIM uses an isotropic shear model while the reference model uses an anisotropic shear model instead. For the lugged wheel (wheel-B), the improvement is even greater; 37.8% improvement due to isotropic shear model and the lugged wheel grouser modeling in WTIM.

These results confirm that WTIM developed in this paper is able to represent wheeled locomotion on deformable soil with appropriate accuracy.

### *4.3. Skid-steering experiment of a wheeled UGV*

By integrating the WTIM-based "wheel–soil model" and the MBS-based "wheel-and-vehicle model," efficient simulation of mobile robots/UGVs in off-road environments can be easily conducted. This fact will be demonstrated by using the UGV experiment reported in refs. [10, 11]. By commanding the left and right wheels with different speeds, the turning trajectory of an 8WD (eight-wheel-drive) skid-steering UGV was recorded by an on-board GPS sensor. The wheel angular speeds and the trajectory of the vehicle center measured in the experiment are given in Figs. 13 and 14, respectively.

The UGV is modeled as a multibody dynamic system by using the *SimMechanics* toolbox in *Simulink*, as shown in Fig. 15. Meanwhile, a WTIM block handles the wheel–soil interaction for each corresponding wheel of the UGV. The WTIM block computes the forces and torques generated by the soil. Compared with the UGV modeling procedure in ref. [11], the tool-based simulation by integrating the WTIM package with the MBS software is more intuitive and flexible.

The soil data and wheel geometry data for the simulation are listed in Table VI. The UGV parameters, which are

[5] One reason for these lower-than-expected R-square values is the scattering of the experimental results between the tests conducted at the same slip angle.

https://doi.org/10.1017/S0263574711000798 Published online by Cambridge University Press

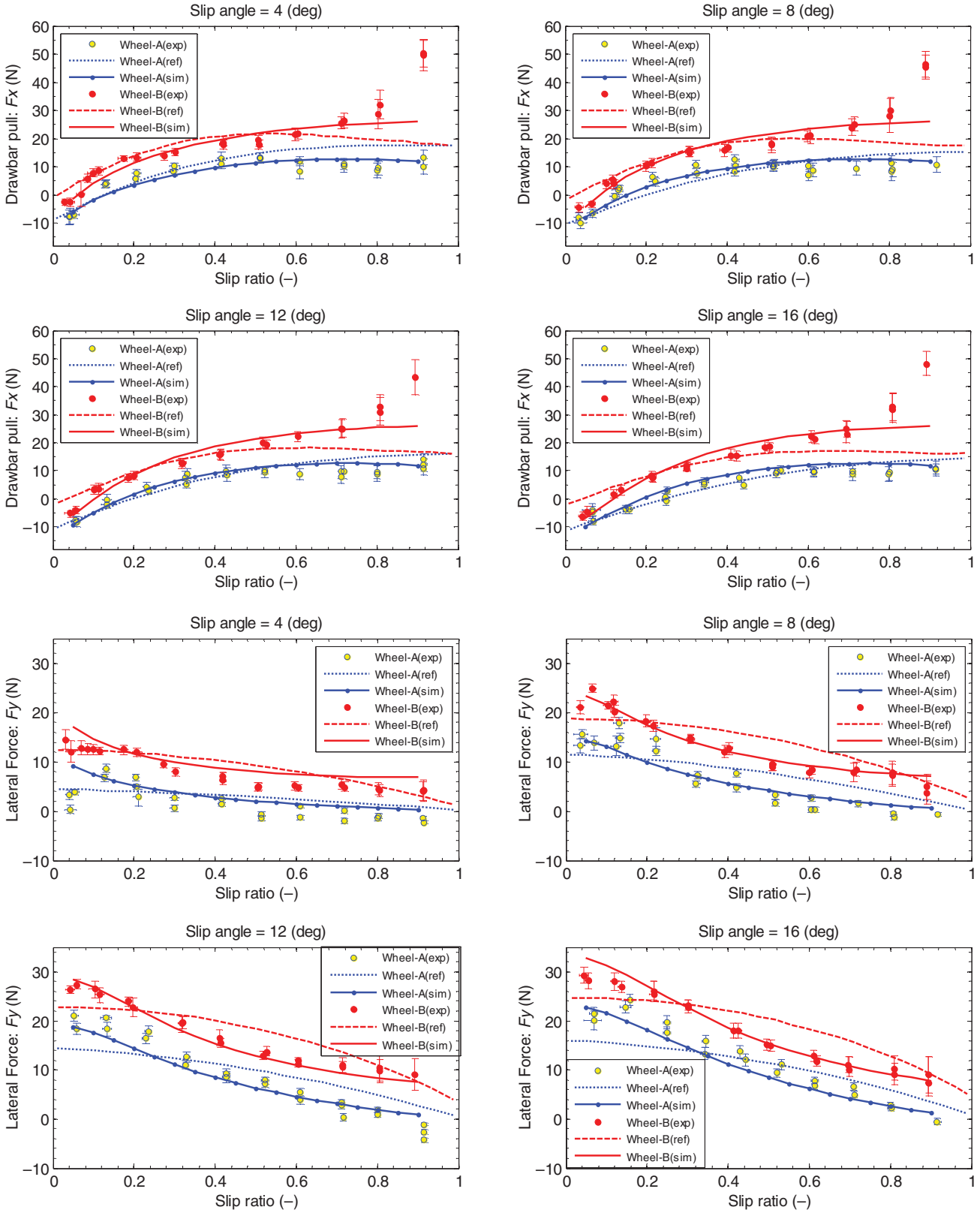


Fig. 12. (Colour online) Results of the single wheel steering experiments. The notations (exp), (ref), and (sim) represent the experiment results, simulation results given in ref. [25], and the simulation results by WTIM, respectively.

required for the simulation, can be found in ref. [11]. The isotropic shear stress approach is used for the simulation. As shown in Fig. 14, the predicted trajectory of the vehicle center agrees well with the experimental data measured by the on-board GPS sensor.

## 5. Conclusions

Based on the theory of terramechanics, a modular, easy-to-use WTIM for off-road vehicle simulations has been developed. The model can be easily integrated with the MBS software to simulate various wheeled

https://doi.org/10.1017/S0263574711000798 Published online by Cambridge University Press

Table VI. Simulation parameters and values for the UGV.

| Parameter | Value | Unit | Description |
|---|---|---|---|
| $\gamma$ | 12.7 | kN/m$^3$ | Soil density |
| $c$ | 4.14 | kPa | Cohesion |
| $\phi$ | 13 | deg | Internal friction angle |
| $n$ | 0.5 | – | Sinkage exponent |
| $k_c$ | 13.19 | kN/m$^{n+1}$ | Cohesive modulus |
| $k_\phi$ | 692.15 | kN/m$^{n+2}$ | Frictional modulus |
| $K$ | 0.006 | m | Shear modulus of the soil |
| $r$ | 0.25 | m | Wheel radius |
| $b$ | 0.246 | m | Wheel width |
| $h_g$ | 0 | mm | Lug height of the grousers |
| $\mu$ | 0 | – | Area ratio of grousers |
| $a_0$ | 0.5 | – | Coefficient for $\theta_m$ |
| $a_1$ | 0.0 | – | Coefficient for $\theta_m$ |
| $b_0$ | 0.0 | – | Coefficient for $\theta_r$ |
| $b_1$ | 0.0 | – | Coefficient for $\theta_r$ |

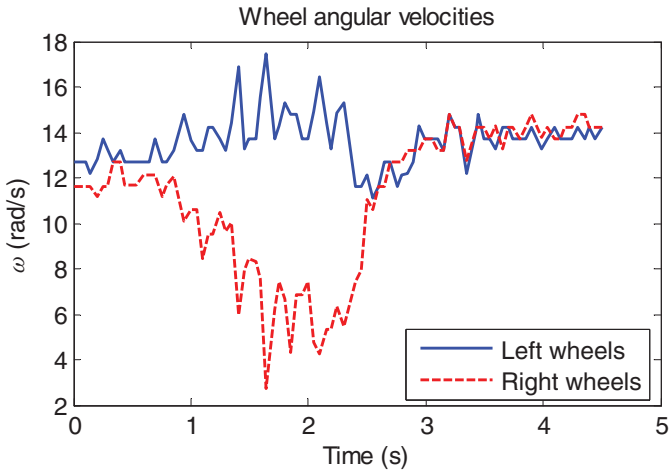


Fig. 13. (Colour online) The left and right wheel angular velocities measured during the UGV steering experiment.[11]

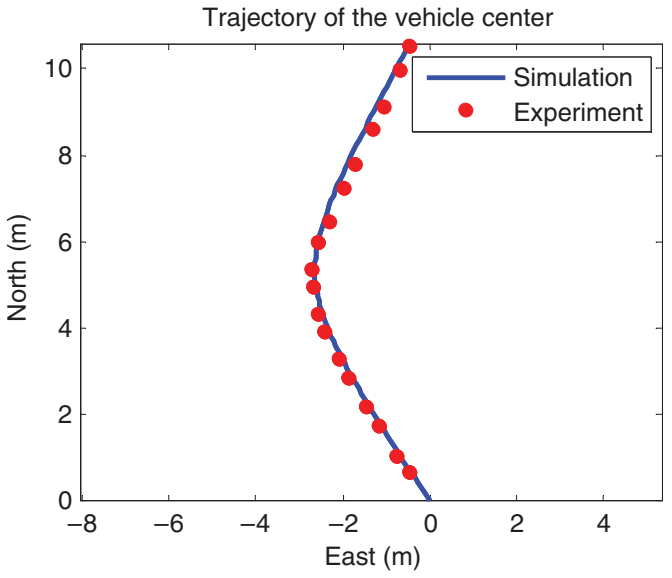


Fig. 14. (Colour online) The UGV trajectory measured in the steering experiment[11] and the simulation results by WTIM and the MBS software.

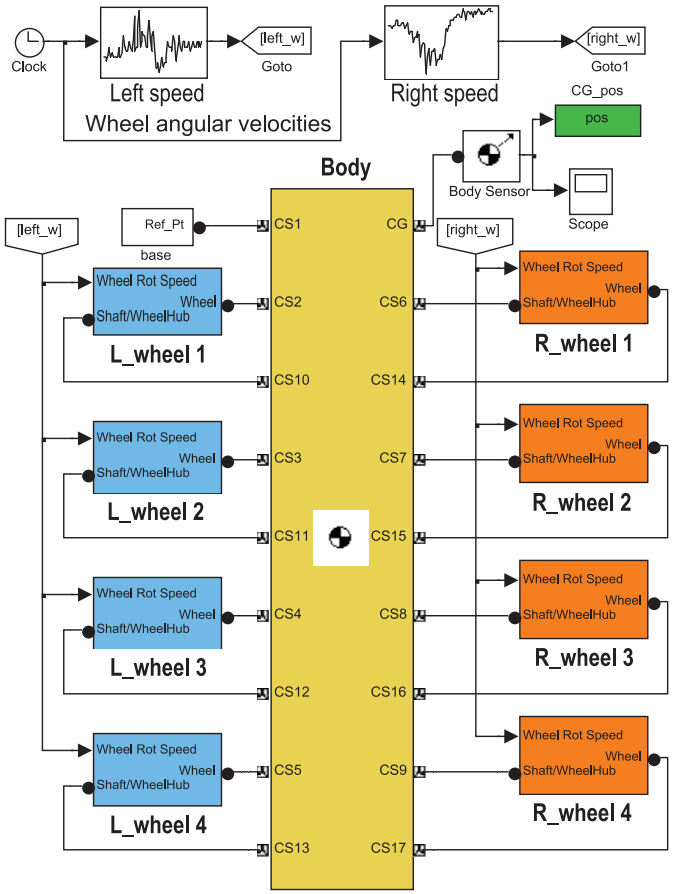


Fig. 15. (Colour online) The 8WD skid-steering UGV modeled in *SimMechanics*. The wheel–soil interaction for each wheel is modeled by a WTIM block. Intuitive and flexible simulation has been achieved by incorporating the WTIM modules with the MBS solver.

vehicles or mobile robots traveling over deformable soil.

The main focus of the model is to identify the stresses along the wheel–soil contact regions, for which some critical aspects have been improved and can be summarized (1) isotropic modeling of the shear stresses underneath the wheel for steering maneuvers; (2) modeling the influence of grousers; (3) modeling the forces and torques contributed by the side surfaces during turning maneuvers.

The model was verified by comparing the simulation results with experimental data reported in the literature, including single-wheel (both straight-line motion and steering maneuvers) experiments and full-vehicle experiments.

## Acknowledgments

This research was supported in part by the Ground Robotics Reliability Center (GRRC) at the University of Michigan, with funding from government contract DoD-DoA W56H2V-04-2-0001 through the Joint Center for Robotics.

## References

1. K. Lagnemma and S. Dubowsky, *Mobile Robot in Rough Terrain*, Springer Tracts in Advanced Robotics, vol. 12 (Springer, Berlin, 2004).

https://doi.org/10.1017/S0263574711000798 Published online by Cambridge University Press

2. J. Morales et al., "Power consumption modeling of skid-steer tracked mobile robots on rigid terrain," *IEEE Trans. Robot.* **25**(5), 1098–1108 (2009).
3. B. Schäfer, A. Gibbesch, R. Krenn and B. Rebele, "Planetary rover mobility simulation on soft and uneven terrain," *Veh. Syst. Dyn.* **48**(1), 149–169 (2010).
4. M. G. Bekker, *Theory of Land Locomotion* (The University of Michigan Press, Ann Arbor, 1956).
5. M. G. Bekker, *Introduction to Terrain-Vehicle Systems* (The University of Michigan Press, Ann Arbor, 1969).
6. J. Y. Wong, *Terramechanics and Off-Road Vehicles* (Elsevier, Amsterdam, 1989).
7. J. Y. Wong, *Theory of Ground Vehicles*, 4th ed. (John Wiley & Sons, Aug. 2008).
8. J. Y. Wong and A. R. Reece, "Prediction of rigid wheels performance based on analysis of soil-wheel stresses, part I. Performance of driven rigid wheels," *J. Terramechanics* **4**(1), 81–98 (1967).
9. J. Y. Wong and C. F. Chiang; "A general theory for skid steering of tracked vehicles on firm ground," *Proc. Inst. Mech. Eng.* **215**(3), 343–355 (2001).
10. T. H. Tran, N. M. Kwok, S. Scheding and Q. P. Ha, "Dynamic Modeling of Wheel-Terrain Interaction of a UGV," *Proceedings of the 3rd Annual IEEE Conference on Automation Science and Engineering*, Scottsdale, AZ, USA (Sep. 22–25, 2007) pp. 369–374.
11. T. H. Tran, "Modeling and Control of Unmanned Ground Vehicles," *Ph.D. Thesis* (Sydney, Australia: The Faculty of Engineering, University of Technology, Sep. 2007).
12. G. Ishigami, A. Miwa, K. Nagatani and K. Yoshida, "Terramechanics-based model for steering maneuver of planetary exploration rovers on loose soil," *J. Field Robot.* **24**(3), 233–250 (2007).
13. G. Ishigami, "Terramechanics-Based Analysis and Control for Lunar/Planetary Exploration Robots," *Ph.D. Thesis* (Sendai, Miyagi, Japan: Department of Aerospace Engineering, Tohoku University, Mar. 2008).
14. I. C. Schmid, "Interaction of vehicle and terrain—Results from 10 years research at IKK," *J. Terramechanics* **32**(1), 3–26 (1995).
15. C. Harnish, B. Lach, R. Jakobs, M. Troulis and O. Nehls, "A new tyre-soil interaction model for vehicle simulation on deformable ground," *Veh. Syst. Dyn.* **43**(1), 384–394 (2005).
16. AESCO, *Matlab/Simulink Module AS*$^2$ *TM User's Guide* (version 1.12) (2005). http:// www.aesco.de/
17. R. Bauer, W. Leung and T. Barfoot, "Experimental and Simulation Results of Wheel–Soil Interaction for Planetary Rovers," *Proceedings of the IEEE/RSJ International Conference on Intelligent Robots and Systems (IROS)*, Shaw Conference Center, Edmonton, Alberta, Canada (Aug. 2–6, 2005) pp. 586–591.
18. M. W. Spong, S. Hutchinson and M. Vidyasagar, *Robot Modeling and Control* (John Wiley & Sons, Nov. 2005).
19. J. M. Solis and R. G. Longoria; "Modeling track-terrain interaction for transient robotic vehicle maneuvers," *J. Terramechanics* **45**(3), 65–78 (2008).
20. J. Liu, H. Gao, Z. Deng and J. Tao, "Effect of Slip on Tractive Performance of Small Rigid Wheel on Loose Sand", *Proceedings of the 1st International Conference on Intelligent Robotics and Applications* (*ICIRA '08*) (2008).
21. L. Ding, H. Gao, Z. Deng, K. Yoshida and K. Nagatani, "Slip Ratio for Lugged Wheel of Planetary Rover in Deformable Soil: Definition and Estimation", *Proceedings of the IEEE International Conference on Intelligent Robots and Systems (IROS '09)*, St. Louis, USA (Oct. 11–15, 2009), pp. 3343–3348.
22. L. Ding, "Wheel–Soil Interaction Terramechanics for Lunar/Planetary Exploration Rovers: Modeling and Application," *Ph.D. Thesis* (Harbin, China: School of Mechatronics Engineering, Harbin Institute of Technology, Dec. 2009).
23. H. Shibly, K. Iagnemma and S. Dubowsky, "An equivalent soil mechanics formulation for rigid wheels in deformable terrain, with application to planetary exploration rovers," *J. Terramechanics* **42**(1), 1–13 (2005).
24. G. Ishigmai, "Locomotion Mechanics for Planetary Exploration Rovers Based on Steering Characteristics," *Master Thesis* (Sendai, Miyagi, Japan: Department of Aerospace Engineering, Tohoku University, Mar. 2005).
25. G. Ishigami, K. Mizuuchi and K. Yoshida, "Terramechanics-Based Analysis on Locomotion Mechanics of Wheeled Mobile Robots (Part 1. Analysis of Wheel Mechanics on Lunar Regolith Simulant)," *Proceedings of the JSME Conference on Robotics and Mechatronics*, Kobe, Japan (Jun. 9–11, 2005).

https://doi.org/10.1017/S0263574711000798 Published online by Cambridge University Press